

Material Flow Visualization in Friction Stir Welding via Particle Tracing

Narges Dialami, Michele Chiumenti, Miguel Cervera

International Center for Numerical Methods in Engineering (CIMNE),
Technical University of Catalonia, Module C1, North Campus
C/ Gran Capitán s/n 08034 Barcelona, Spain.

Corresponding author: Narges Dialami Tel.(+34) 93 401 6529 / Fax.(+34) 93 401 6517

E-mail addresses: narges@cimne.upc.edu (N. Dialami),
michele@cimne.upc.edu (M. Chiumenti), mcervera@cimne.upc.edu (M. Cervera)

Abstract

This work deals with the modeling of the material flow in Friction Stir Welding (FSW) processes using particle tracing method. For the computation of particle trajectories, three accurate and computationally efficient integration methods are implemented within a FE model for FSW process: the Backward Euler with Substepping (BES), the 4-th order Runge-Kutta (RK4) and the Back and Forth Error Compensation and Correction (BF ECC) methods. Firstly, their performance is compared by solving the Zalesak's disk benchmark. Later, the developed methodology is applied to some FSW problems providing a quantitative 2D and 3D view of the material transport in the process area. The material flow pattern is compared with the experimental evidence.

Keywords: Friction Stir Welding, Material flow, Particle tracing, BES, BF ECC, RK4

1. Introduction

Friction Stir Welding is a solid-state joining technique lately found by Thomas et. Al. [1]. A schematic representation of the FSW process is illustrated in Figure 1. A shouldered pin rotating at constant rotational speed is inserted into the line between the two plates to be welded. Once the insertion is completed, the pin is moved along the welding line at constant rotating and advancing speeds to form the joint. The joining is achieved via the generated heat and the material mixing/stirring process.

The heat is induced both by the friction between the tool shoulder and the workpieces and by the plastic dissipation in the process area. On one hand, the shoulder is essential to generate heat through the friction process and to prevent the expulsion of the material during the movement of the pin-tool. On the other hand, the pin deforms the material around it generating heat by plastic dissipation. The quality of the final joint, as well as the final microstructure of the material, depends on both mechanisms: the shoulder must generate heat enough to allow for the material to flow around the tool and to obtain a deep heat affected zone (HAZ). Insufficient heat is usually due to insufficient normal pressure or an incorrect shoulder diameter. Consequently, the material is not softened enough for it to flow properly and voids are formed. Moreover, the pin-tool shape as well as the welding parameters (such as the advancing and rotating speed) can significantly affect the material flow pattern modifying the mechanical properties of the joint [2]. In the FSW process, the plastic deformation concentrates nearby the pin. The extent of the stir-zone plays a critical role for the quality of the

joint-strength. To achieve a high quality and defect-free weld, it is necessary to produce a deep penetrating stir-zone around the pin.

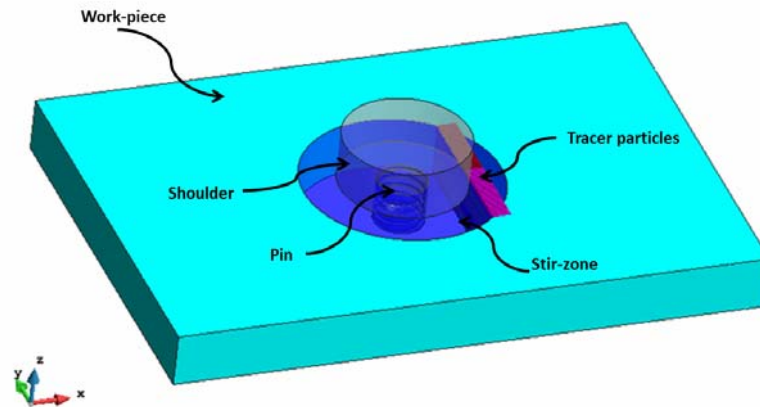


Figure 1: Schematic description of the different tools in a FSW process

The visualization of the material flow is very useful to understand the size of the stir-zone and its penetration within the thickness of the welding plate. However, following the position of the material during the welding process is not an easy task, neither experimentally or numerically.

Experimentally, the motion of the material in the stir-zone is usually tracked using the so-called Marker Insert Technique (MIT). The markers, made from a different material to the plate, are inserted into the welding line and their final positions (after the welding process) are detected by means of a metallographic study or X-ray radiography. Different contrast materials are used as markers: Al-alloys [3, 4, 5], steel balls [6], copper foils [7, 8], plasticine and brass rods [9].

Another possibility to visualize the material mixing consists of welding two dissimilar materials. This technique enables an easy visualization of the material redistribution at the joint interface. The two materials can be different magnesium alloys [10], aluminum or copper alloys [11], [12].

The material located close to the pin-tool undergoes a vertical movement induced by the threaded pin shape while rotating from the advancing to the retreating side of the pin tool. Experimentally, it is very difficult to track the material flow within the thickness of the stir-zone.

The alternative is the development of numerical techniques able to simulate the FSW process in all its complexity together with an ad-hoc material tracing technology. This paper is a step forward in this direction, within the field of FSW simulation where a fully thermo-mechanical Finite Element model has been developed within the Arbitrary-Lagrangian-Eulerian kinematic framework (a detailed description of this work can be found in [13, 14]). The purpose of the current work is to get a better understanding of the material behavior due to the stirring process. The trajectories of the stirred material are computed and visualized using different particle tracing techniques. This methodology, widely used in image processing or in fluid dynamics analysis, is a suitable and robust tool to study the FSW problem allowing for a clear visualization of the material movement at the stir-zone leading to a better understanding of the welding process itself.

A brief description resuming the main aspects of the simulation technology used for the numerical analysis of the FSW process is presented in Section 2. Section 3 describes different time integration schemes allowing for the particle tracing analysis: the Backward Euler with Sub-stepping (BES), 4-th order Runge-Kutta (RK4) and the Back and Forth Error Compensation and Correction (BFEC) method. In the last Section the different techniques for the material tracing are compared and then used for 2D and 3D FSW simulations.

2. FSW simulation technology

In this section the main characteristics of the FSW model are briefly explained. In the FSW process the pin rotates at a constant angular velocity and, at the same time, it moves forward at constant advancing speed. The work-piece (i.e. the sheet plate to be welded) is clamped to the back-plate. Consequently, the simulation analysis defines pure rotation (around a fix rotation axis) for the pin while the advancing speed (in the opposite direction) is assigned to both the work-piece and the back-plate. This given, the main idea to simulate the FSW process consists of dividing the original geometry into three different zones which are: the pin, the work-piece (excluding the process-zone close to the pin) and the stir-zone (process/welding zone) also referred to as Heat Affected Zone (HAZ). In each domain, the most suitable kinematic framework is considered. The work-piece is modeled in the Eulerian framework assuming an in-flow velocity, which corresponds to the advancing speed of the pin-tool. The pin is assumed to be rigid: its rotation is described in Lagrangian framework. Finally, the Arbitrary-Lagrangian-Eulerian (ALE) kinematic framework is used to study the stir-zone. The main reason for this split is, on one hand, that the large deformations (material stirring) in the process zone cannot be easily handled with a classical updated Lagrangian scheme, since it leads to excessive mesh distortions. To overcome the degradation of the results, the Lagrangian framework should be complemented by a continuous re-meshing strategy. On the other hand, a purely Eulerian scheme is also difficult to apply due to the change in the boundary conditions induced by the rotation of the pin. Therefore, the choice of ALE kinematic framework is very convenient because re-meshing is not necessary and moving boundaries can be easily taken into account. In fact, the mesh representing the work-piece is kept fix (Eulerian description), while the mesh of the pin and the stir-zone is rigidly rotated according to the angular velocity defined for the FSW process. As a consequence, the pin (rigid) is described in Lagrangian framework (the mesh strictly follows the body movement) while, in the stir-zone, the actual velocity field and the imposed mesh movement are different (ALE hypothesis).

Note that the ALE framework is very general, including both Lagrangian and Eulerian settings as particular cases. In the following, the governing equations of the thermo-mechanical problem used to solve the FSW problem will be presented in this format (more details in [13,14]).

From the constitutive point of view, the main hypotheses adopted for the numerical simulation of the FSW process are:

- Both the stress tensor, $\boldsymbol{\sigma}$, and the strain rate tensor, $\dot{\boldsymbol{\epsilon}}$, admit a similar split into volumetric and deviatoric parts:

$\boldsymbol{\sigma} = p\mathbf{1} + \mathbf{s}$	(2.1)
--	-------

$\dot{\boldsymbol{\epsilon}} = \frac{1}{3}\dot{\epsilon}_{vol}\mathbf{1} + \dot{\boldsymbol{\epsilon}}$	(2.2)
---	-------

where p and \mathbf{s} are the pressure and the stress deviator, respectively. Similarly, \dot{e}_{vol} and $\dot{\mathbf{e}}$ are the volumetric and deviatoric parts of the strain rate tensor, respectively.

- The deviatoric part of total strain rate tensor, $\dot{\mathbf{e}}$ is computed as the symmetric gradient of the velocity field as: $\dot{\mathbf{e}} = \text{dev}(\dot{\boldsymbol{\epsilon}}) = \nabla^s \mathbf{v}$. This means that the volumetric deformation, $\dot{e}_{vol} = \nabla \cdot \mathbf{v} \cong 0$, including thermal deformation, is negligible. Therefore, the material rate flow is assumed to be incompressible.

- Due to the high viscosity of the material and, consequently, the very low values of Reynolds number in the FSW analysis, the inertia term of the balance of momentum equation can be neglected. Therefore, the mechanical problem is solved within the hypothesis of quasi-static analysis.

This given, the governing equations in ALE format (balance of momentum, mass conservation and balance of energy) which describe the thermo-mechanical problem are:

$$\begin{cases} \nabla \cdot \mathbf{s} + \nabla p + \rho_o \mathbf{b} = \mathbf{0} \\ \nabla \cdot \mathbf{v} = 0 \\ \rho_o c \left[\frac{\partial T}{\partial t} + (\mathbf{v} - \mathbf{v}_{mesh}) \cdot \nabla T \right] = D_{mech} - \nabla \cdot \mathbf{q} \end{cases} \quad (2.3)$$

where ρ_o , \mathbf{b} and c are the density, the body forces per unit of mass and the specific heat, respectively. D_{mech} is the dissipation rate per unit of volume due to the plastic work. The heat flux, \mathbf{q} , is defined according to the isotropic Fourier's law as:

$$\mathbf{q} = -k \nabla T \quad (2.4)$$

where k is the thermal conductivity and T is the temperature field.

The mesh velocity is denoted by \mathbf{v}_{mesh} . Observe that the convective term $\rho_o c (\mathbf{v} - \mathbf{v}_{mesh}) \cdot \nabla T$ vanishes in the Lagrangian framework ($\mathbf{v} = \mathbf{v}_{mesh}$) and reduces to $\rho_o c \mathbf{v} \cdot \nabla T$ in the Eulerian zone ($\mathbf{v}_{mesh} = \mathbf{0}$).

The boundary conditions to complete the coupled problem (2.3) are generally defined for the mechanical analysis in term of prescribed in-flow velocity, at one end of the work-piece, and rotational velocity assigned to the pin-tool. Both velocities are the most representative parameter to be studied in the FSW analysis. Referring to the thermal problem, neither Dirichlet nor Neumann boundary conditions are usually applied. Instead, the thermal analysis is completed defining the heat flow dissipated through the boundaries by heat convection (Newton's law) and heat radiation processes:

$$\begin{cases} q_{conv} = h_{conv} (T - T_{env}) \\ q_{rad} = \sigma_0 \varepsilon (T^4 - T_{env}^4) \end{cases} \quad (2.5)$$

where h_{conv} is the heat transfer coefficient by convection, σ_0 is the Stefan–Boltzmann constant and ε is the emissivity factor. Finally, T_{env} is the surrounding environment temperature.

In FSW, the heat necessary for the welding process is generated both by the plastic dissipation due to the material stirring in the process zone and by the friction process at the contact interface between the shouldered pin-tool and the work-piece surface.

On one hand, the mechanical dissipation is computed as:

$$\dot{D}_{mech} = \gamma \mathbf{s} : \dot{\mathbf{e}} \quad (2.6)$$

where $\gamma \approx 90\%$ is the fraction of the total plastic energy which is converted into heat. Observe that the constitutive model chosen is rigid-visco-plastic: the elastic

deformations are negligible if compared with the total amount of plastic strains developed in the stir-zone. The constitutive relationship between the (deviatoric) stress tensor and the (plastic) strain rate is defined in the following general format as:

$$\mathbf{s} = 2\mu_{eff} \dot{\mathbf{e}} \quad (2.7)$$

where the effective viscosity, $\mu_{eff}(\|\dot{\mathbf{e}}\|, T)$, is determined according to the rigid-viscoplastic constitutive law chosen (i.e. Norton–Hoff or Sheppard–Wright models).

Besides, the heat flux produced by the frictional contact between pin and the work-piece is expressed by the Norton’s friction model as:

$$\begin{cases} q_{frict}^{pin} = \mathcal{G}^{pin}(\mathbf{t}_T \cdot \Delta \mathbf{v}_T) = \mathcal{G}^{pin} a(T) \|\Delta \mathbf{v}_T\|^{q+1} \\ q_{frict}^{SZ} = \mathcal{G}^{SZ}(\mathbf{t}_T \cdot \Delta \mathbf{v}_T) = \mathcal{G}^{SZ} a(T) \|\Delta \mathbf{v}_T\|^{q+1} \end{cases} \quad (2.8)$$

where the amount of heat absorbed by the pin-tool, \mathcal{G}^{pin} , and by the work-piece, \mathcal{G}^{SZ} , (at the stir-zone) depends on the thermal diffusivity, $\alpha = \frac{k}{\rho_o c}$, of the two materials in

contact as:

$$\begin{cases} \mathcal{G}^{pin} = \frac{\alpha^{pin}}{\alpha^{pin} + \alpha^{SZ}} \\ \mathcal{G}^{SZ} = \frac{\alpha^{SZ}}{\alpha^{pin} + \alpha^{SZ}} \end{cases} \quad (2.9)$$

The tangential component of the traction vector at the contact interface, \mathbf{t}_T , is defined using the Norton’s friction law as:

$$\mathbf{t}_T = a(T) \|\Delta \mathbf{v}_T\|^q \mathbf{u}_T \quad (2.10)$$

where $a(T)$ is the (temperature dependent) material consistency, $0 \leq q \leq 1$ is the strain rate sensitivity and $\mathbf{u}_T = \frac{\Delta \mathbf{v}_T}{\|\Delta \mathbf{v}_T\|}$ is the tangential unit vector, defined in terms of the relative tangential velocity at the contact interface, $\Delta \mathbf{v}_T$.

The weak form of the FSW problem (2.3) defined over the integration domain Ω and its boundary $\partial\Omega$ reads as:

$$\begin{cases} \int_{\Omega} (\mathbf{s} : \nabla^s \delta \mathbf{v}) dV + \int_{\Omega} (p \nabla \cdot \delta \mathbf{v}) dV = W_{mech} & \forall \delta \mathbf{v} \\ \int_{\Omega} [(\nabla \cdot \mathbf{v}) \delta p] dV = 0 & \forall \delta p \\ \int_{\Omega} \left(\rho_o c \left[\frac{\partial T}{\partial t} + (\mathbf{v} - \mathbf{v}_{mesh}) \cdot \nabla T \right] \delta T \right) dV + \int_{\Omega} [k \nabla T \cdot \nabla (\delta T)] dV = W_{ther} & \forall \delta T \end{cases} \quad (2.11)$$

where the mechanical and the thermal work of the external forces is defined as:

$$\begin{cases} W_{mech} = \int_{\Omega} (\rho_o \mathbf{b} \cdot \delta \mathbf{v}) dV \\ W_{ther} = \int_{\Omega} (\dot{D}_{mech} \delta T) dV + \int_{\partial\Omega} [(q_{conv} + q_{rad}) \delta T] dS \end{cases} \quad (2.12)$$

The test functions of the velocity, pressure and temperature fields are $\delta \mathbf{v}$, δp and δT , respectively.

The discrete FE counterpart of the weak form (2.11) is solved using (stable) mixed v - p - T finite elements with linear interpolations for all the nodal variables. To overcome the limitations on the choice of the interpolation spaces imposed by the Ladyzhenskaya–Babuška–Brezzi (LBB) inf-sup condition [23], the proposed formulation is stabilized using Orthogonal Sub-Grid Scale method (OSS). More details related to the mixed finite element technology to deal with the incompressibility constraint in both linear and non-linear problems can be found in [24, 25, 26].

Finally, the coupled thermo-mechanical problem is solved by means of staggered time-marching scheme where two sub-problems (thermal and mechanical) are solved sequentially, within the framework of the classical fractional step methods [21,22].

3. Particle tracing

Particle tracing is a method used to simulate the motion of particles (tracers), following their positions at each time-step of the analysis. The method can be naturally applied to the study of the material flow around the pin in FSW process.

Let us assume that the velocity field, $\mathbf{v}_j(t)$, is known at each node, j , of the finite element mesh representing the domain at any time, t , of the analysis. The position of a generic tracer at the same instant of time, $\mathbf{X}(t)$, can be computed by solving the following differential equation at each time-step of the analysis:

$$\frac{D(\mathbf{X}(t))}{Dt} = \mathbf{V}(\mathbf{X}(t), t) \quad (3.1)$$

Integrating:

$$\mathbf{X}(t) = \mathbf{X}_0 + \int_0^t \mathbf{V}(\mathbf{X}(t), t) dt \quad (3.2)$$

where \mathbf{X}_0 is the initial position of the particle (see Figure 1). $\mathbf{V}(\mathbf{X}(t), t)$ is the velocity of the tracer at its current position. This velocity can be computed in two steps: firstly, it is necessary to know in which element (of the FE discretization of the plate) the tracer is contained (a spatial search algorithm¹ is required) and, secondly, its velocity is interpolated from the values of the velocity field at the nodes of this element and the corresponding interpolation (shape) functions, $N^j(\mathbf{X}(t))$, as:

$$\mathbf{V}(\mathbf{X}(t), t) = \sum_{j=1}^n \mathbf{v}_j(t) \cdot N^j(\mathbf{X}(t)) \quad (3.3)$$

The solution of the ordinary differential equation (ODE) (3.1) returns the sequence of positions, $\mathbf{X}(t_n)$ for all the tracers according to the time-marching scheme of the analysis. The post-process of this solution defines the trajectories of all the tracers originally placed in the stir-zone.

A large number of time integration schemes have been developed up to date to solve equation (3.1). These methods range from the simple first order Backward Euler (BE) scheme to higher order Runge-Kutta schemes. In this work, the following integration schemes are compared for the particle tracing in the FSW process: BE with Sub-stepping (BES), the 4-th order Runge-Kutta (RK4) and the Back and Forth Error Compensation and Correction method (BFEC).

¹ In the present work, the bins algorithm is used.

BE with Sub-stepping

This method is a refinement of the classical BE scheme. Let us assume that the velocity field is known at time t_n and t_{n+1} . Using the BE scheme, the position of a generic tracer $\mathbf{X}_{n+1} = \mathbf{X}(t_{n+1})$ is computed as:

$$\begin{cases} \mathbf{X}_{n+1} = \mathbf{X}_n + \int_{t_n}^{t_{n+1}} \mathbf{V}(\mathbf{X}(t_{n+1})) dt \\ \cong \mathbf{X}_n + \mathbf{V}(\mathbf{X}(t_{n+1})) \Delta t = \mathbf{X}_n + \mathbf{V}_{n+1} \Delta t \end{cases} \quad (3.4)$$

where the size of the time-step interval is $\Delta t = t_{n+1} - t_n$.

If a *sub-stepping* technique is added, then the method transforms into:

$$\begin{cases} \mathbf{X}_{n+1} \cong \mathbf{X}_n + \sum_{i=1}^k \mathbf{V}_{n+1}^i \delta t^i \\ \delta t^i = \frac{\Delta t}{k} \end{cases} \quad (3.5)$$

where Δt is split into k sub-steps. The velocity field, \mathbf{v}_{n+1}^i , corresponding to the generic sub-step i is obtained as:

$$\begin{cases} \mathbf{v}_{n+1}^i(t) = (1 - \tau_t) \mathbf{v}_n + \tau_t \mathbf{v}_{n+1} \\ \tau_t = \frac{t - t_n}{t_{n+1} - t_n} \quad t_n < t < t_{n+1} \end{cases} \quad (3.6)$$

The velocity of the tracer, \mathbf{V}_{n+1}^i , is computed in two steps: firstly, its position $\mathbf{X}_{n+1}^i = \mathbf{X}\left(t_n + \sum_{i=1}^k \delta t^i\right)$ is updated according to the results obtained in the previous sub-steps; secondly, the velocity of the tracer is interpolated from the velocity field computed at the mesh nodes of the work-piece (see Figure 2).

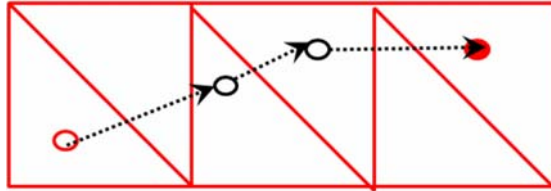


Figure 2: Position of the tracer at each sub-step

Remark: The BES method is first order accurate $O(\Delta t)$, even if a large number of sub-steps is considered.

3.1. BFECC method

The BFECC method is a well-known technique mostly used for weather forecast. It was first proposed in [15] with the aim of reducing mass loss in level set methods (see [16], [17]).

Denoting with $A(\cdot)$ the first order up-winding integration operator defined by equation (3.2), BFECC consists of a prediction/correction procedure: the initial position of the tracer, $\mathbf{X}_n = \mathbf{X}(t_n)$, is advected forward to $\hat{\mathbf{X}}_{n+1} = A(\mathbf{X}_n)$, and then backward to

$\hat{\mathbf{X}}_n = A^R(\hat{\mathbf{X}}_{n+1})$, being $A^R(\cdot)$ the backward advection operator. The difference between $\hat{\mathbf{X}}_n$ and the initial position defines the error, \mathbf{e} , of the time integration scheme:

$$\mathbf{e} = \frac{1}{2}(\mathbf{X}_n - \hat{\mathbf{X}}_n) \quad (3.7)$$

This error is used later to correct the starting position, $\bar{\mathbf{X}}_n = \mathbf{X}_n + \mathbf{e}$, for the next advection step, achieving the final solution, $\mathbf{X}_{n+1} = A(\bar{\mathbf{X}}_n)$.

The steps of the BFECC method can be written as follows (see Figure 3):

$$\begin{cases} \hat{\mathbf{X}}_{n+1} = A(\mathbf{X}_n) \\ \hat{\mathbf{X}}_n = A^R(\hat{\mathbf{X}}_{n+1}) \\ \bar{\mathbf{X}}_n = (\mathbf{X}_n + \hat{\mathbf{X}}_n)/2 \\ \mathbf{X}_{n+1} = A(\bar{\mathbf{X}}_n) \end{cases} \quad (3.8)$$

Remark 1: The BFECC method is 3-rd order accurate, meaning that the error per step is $O(\Delta t^4)$, while the total accumulated error is $O(\Delta t^3)$

Remark 2: Operator $A(\mathbf{X})$ involves the computation of the velocity field of the tracer in its current position, so that it is necessary to interpolate it from the nodal values of the FE mesh at each step of the algorithm.

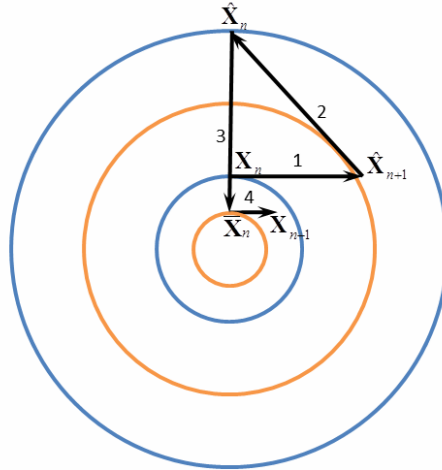


Figure 3: The steps of the BFECC method for a rotational velocity field

3.2. RK4 method

A very powerful class of integration methods belongs to the Runge-Kutta multi-step family. Using the 4-th order Runge-Kutta method, the approximation of the function $\mathbf{X}(t_{n+1}) = \mathbf{X}_{n+1}$, is determined by the present value $\mathbf{X}(t_n) = \mathbf{X}_n$ plus the weighted average of four incremental displacements computed as the product of the size of the interval, Δt , and an estimated velocity, $\mathbf{V}(\mathbf{X}(t), t)$, defined by the right-hand side of the differential equation (3.1). More specifically:

- $\Delta \mathbf{X}^{(1)} = \mathbf{V}(\mathbf{X}_n, t_n) \Delta t$ is the incremental displacement based on the velocity at the beginning of the interval, using \mathbf{X}_n , (Euler's method) ;

- $\Delta\mathbf{X}^{(2)} = \mathbf{V}\left(\mathbf{X}_n + \frac{1}{2}\Delta\mathbf{X}^{(1)}, t_n + \frac{\Delta t}{2}\right)\Delta t$ is the incremental displacement based on the velocity at the midpoint of the interval, using $\mathbf{X}_n + \frac{1}{2}\Delta\mathbf{X}^{(1)}$;
- $\Delta\mathbf{X}^{(3)} = \mathbf{V}\left(\mathbf{X}_n + \frac{1}{2}k_2, t_n + \frac{\Delta t}{2}\right)\Delta t$ is again the incremental displacement based on the velocity at the midpoint, but now using $\mathbf{X}_n + \frac{1}{2}\Delta\mathbf{X}^{(2)}$;
- $\Delta\mathbf{X}^{(4)} = \mathbf{V}(\mathbf{X}_n + k_3, t_n + \Delta t)\Delta t$ is the incremental displacement based on the velocity at the end of the interval, using $\mathbf{X}_n + \Delta\mathbf{X}^{(3)}$.

The four increments chosen are weighted according to the classical Simpson's integration rule and the result is:

$\mathbf{X}_{n+1} = \mathbf{X}_n + \frac{1}{6}(\Delta\mathbf{X}^{(1)} + 2\Delta\mathbf{X}^{(2)} + 2\Delta\mathbf{X}^{(3)} + \Delta\mathbf{X}^{(4)})$	(3.9)
--	-------

Remark 1: The RK4 method is a 4-th order method, meaning that the error per step is $O(\Delta t^5)$, while the total accumulated error is $O(\Delta t^4)$.

Remark 2: The RK4 method achieves exact integration of a circular trajectory; this is the most common material path in FSW.

4. Numerical simulations

The examples of this section are chosen in order to demonstrate:

- The performance of the integration techniques described in the previous section, in application to the particle trajectories simulation.
- The suitability of the proposed method for the visualization of material flow around the threaded pin comparing a 2D case with experimental data and extending the work to a 3D case.

4.1. Particle tracing for Zalesak's Disk

This example deals with the two-dimensional problem of a rigid body rotation and aims at comparing the particle tracing method using different time schemes such as RK4, BFECC, BES and BE. The two-dimensional Zalesak's Problem [19] can be described as follows. The integration domain is a circular area with center at (50,50) and radius of 50. Within this area the velocity is prescribed as a rotational field with constant angular velocity. A cutout circular disk centered at (50,75) with radius 15 is defined as a set of particles immersed in the prescribed velocity field. The slot being cut out has a width of 5 and length of 25. The rotational velocity field is prescribed as $(u, v) = \left(\frac{\Pi}{314}(50 - y), \frac{\Pi}{314}(x - 50) \right)$. Every point of the cutout circle is transported by the local velocity field where the rotation takes place.

The time step and rotational speed are chosen such that 628 time steps complete one revolution of the disk.

The FE mesh used to define the velocity field of the integration domain as well as the set of particle forming the disk is shown in Figure 4. The whole model is discretized with a mesh of approximately 18000 triangular elements, 10000 points and 700 particles. In the first trial, the problem is solved with $n = 314$ time steps and $\Delta t = 2$.

The results of different integration methods (RK4, BFECC and BES for 10 sub-steps) are shown after first revolution in Figure 5, together with the original position. It can be clearly seen that after the first revolution, the cutout disk returns to the original position with an imperceptible error for all three integration methods. Nevertheless, the difference becomes more visible after several revolutions. Figure 6 shows the disk position after completing 10 revolutions. The resulting error using RK4 and BFECC methods is still negligible. However, RK4 shows a slightly better result. The resulting error using BE and BES is considerable. The BE results to be unacceptable (huge computational error) as the particles expand and stick to the domain boundary.

In the second trial, the problem is computed with a larger time step, performing 10 revolutions. The number of time steps is $n = 628$, using the time interval $\Delta t = 10$. The results are illustrated in Figure 7. The results are ranked, according to computational error, as RK4, BFECC, BES and BE. Note that with a larger time step, RK4 maintains an adequate accuracy of the results, while BFECC becomes inaccurate for the large time steps. The BE methods fail for this value of time step.

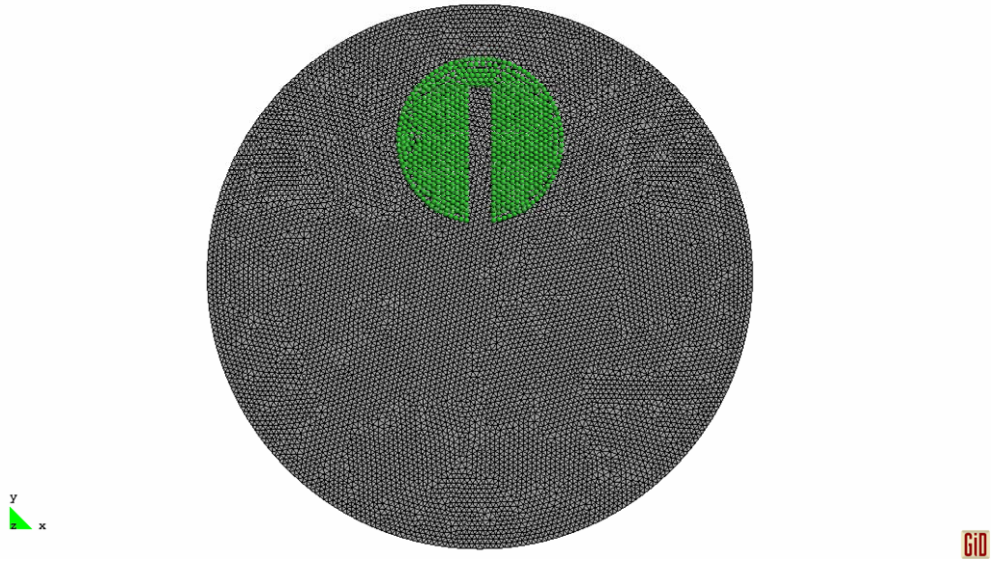


Figure 4: Background mesh

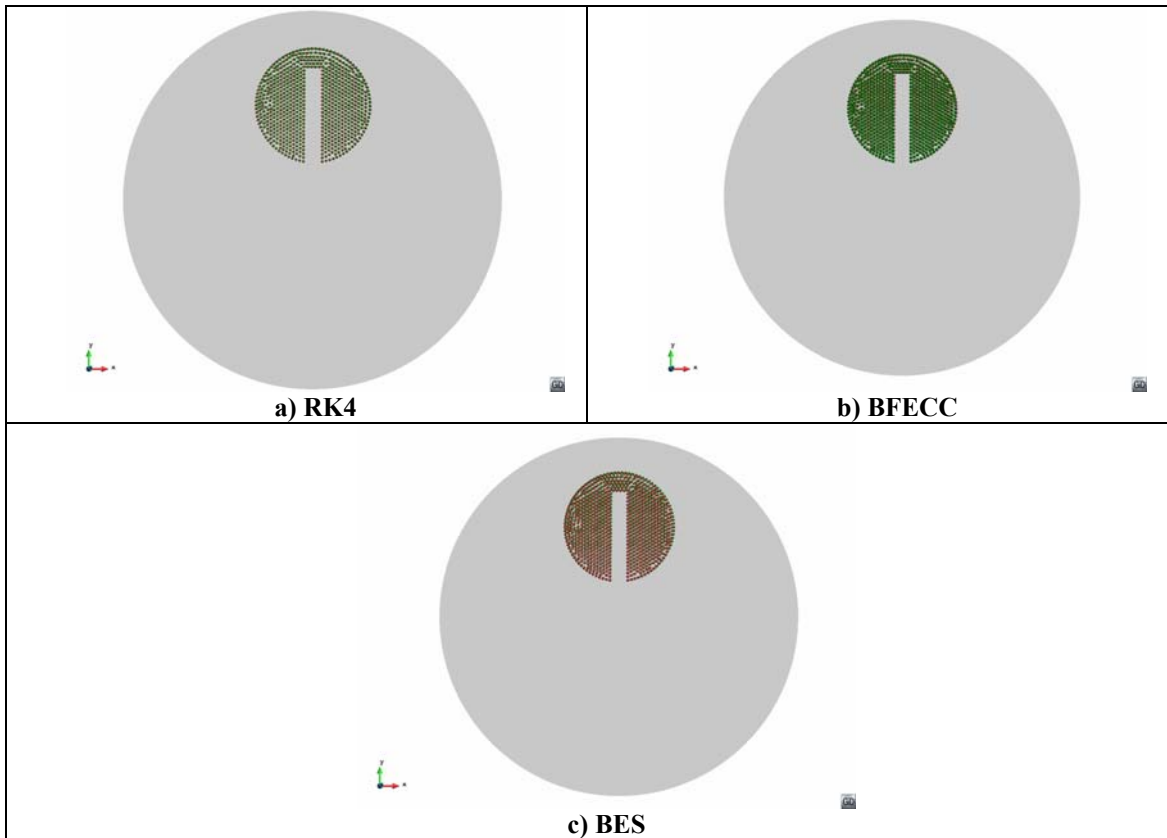


Figure 5: First revolution of the cutout disk

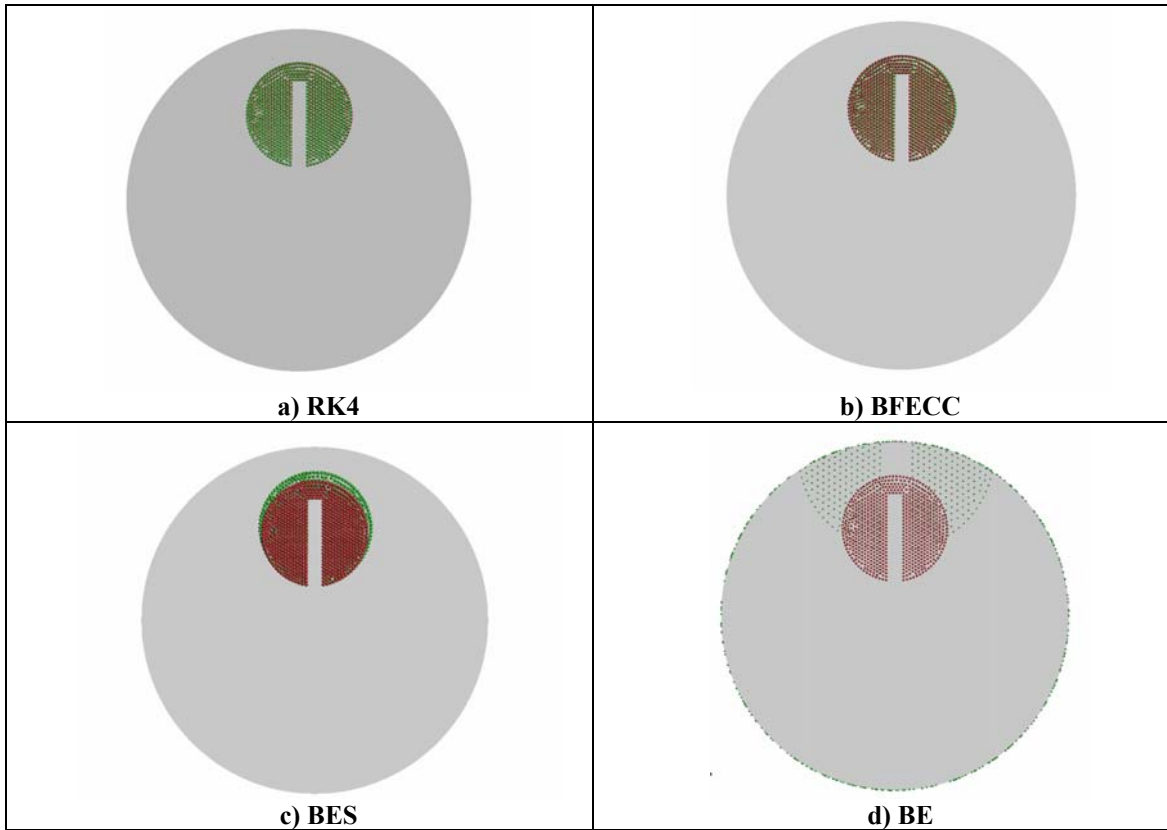


Figure 6: 10 revolutions of the cutout disk with time-step= 2 s

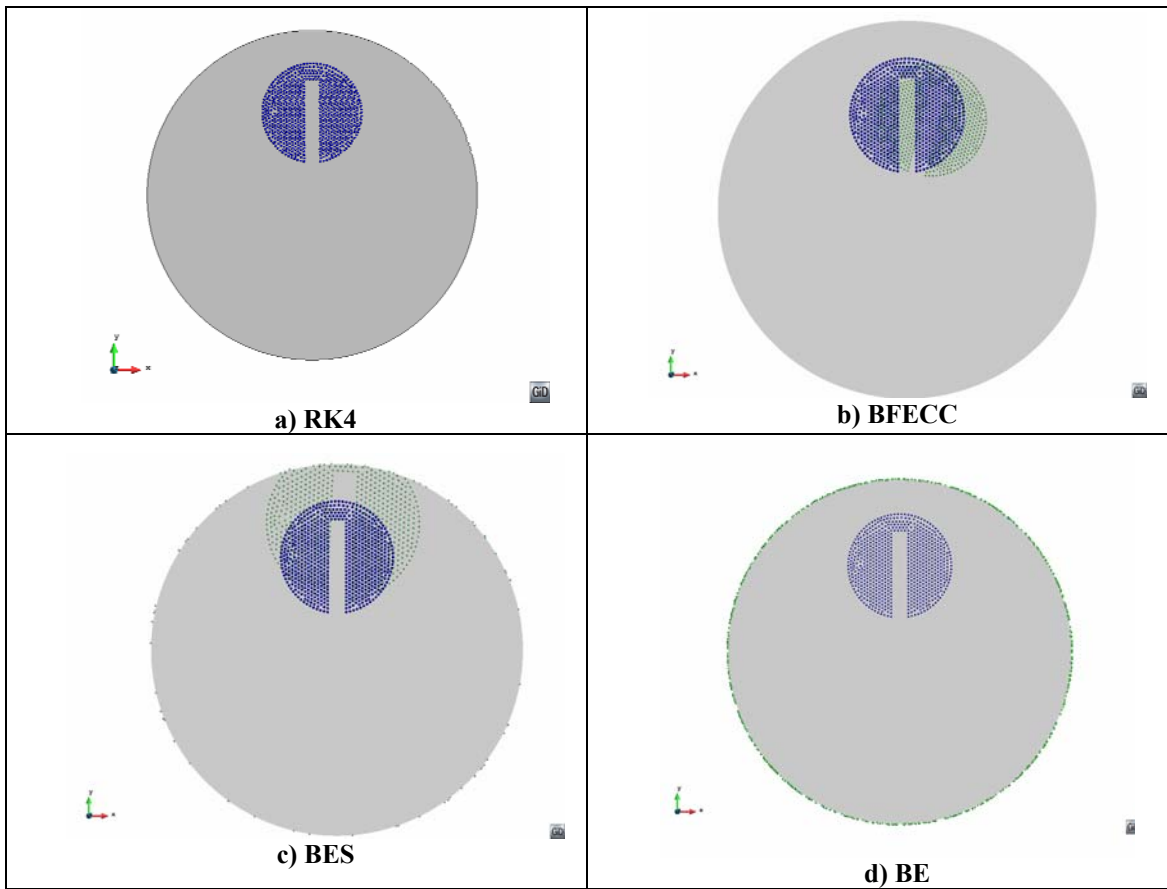


Figure 7: 10 revolutions of the cutout disk with time-step= 10 s

4.2. FSW simulation

The objectives of this section are, on one side, to validate the work comparing the numerical results with the experimental data, and, on the other side, to study the material mixing during the FSW process.

The modeling and simulations are based on the experimental work by Reynolds et al. [20]. The friction stir welds investigated in this work consist of welded plates 1.8 mm thick. A tool consisting of a threaded pin with 9.9 mm of diameter and a shoulder with 25.4 mm of diameter was used. In the experiment, the markers used were thin sheets of 5454 Al. They were inserted in AA2195-T8 Al plates at various depths on both the advancing and retreating sides of the weld. Process parameters were: welding speed $V_s = 5.0833$ mm/s and rotational speed $V_r = 500$ rpm. After welding was completed, the work-piece was thinned by mechanical milling in steps, and after each step, the work-piece was polished revealing the position of the 5454 Al marker material. After processing of welded cross-sections, an interface between the two sides of the weld was apparent. The marker positions were digitized and combined into three-dimensional maps indicating the flow.

4.2.1. FSW 2D simulation

In order to show the ability of the proposed procedure for the visualization of material flow around the pin, a 2D-case of the simplified FSW simulation is considered. The model is a transversal cut of the pin, with 10 mm of diameter, perpendicular to the rotation axis. The cut represents the mid-section of the real threaded pin. The contact condition between the pin and the work-piece is considered to be full stick. Process parameters are the same as in the experiment: welding speed $V_s = 5.0833$ mm/s and rotational speed $V_r = 500$ rpm. A Sheppard-Wright constitutive model is used. The model and the parameters are summarized in the Table 1.

A set of 5500 particles in a shape of a 2×60 mm rectangle at their initial position is located right in front of the pin. The whole model is discretized with a mesh of 4986 triangular elements. The problem is solved using the \mathbf{u}/p mixed formulation stabilized by the OSS stabilization method [13, 14]. RK4 time integration method is applied for the solution of the particle tracing problem.

Figure 8 shows the final position of the particles compared with the experimental results at the mid-section of the pin taken from Reynolds [20] (AS and RS stand for advancing side and retreating side, respectively). The flow pattern is visualized after 4 s, the time that the particles spend to cross the pin. The pin rotation produces heat by viscoplastic deformation in the work-piece, decreasing the flow stress of the material. Consequently, the material in the weld zone flows. The material is moved to a final position behind its original position; only small amount of material on the advancing side is shifted to a final position in front of its original position.

The results show that the numerical particle tracing reveals characteristic patterns of material flow in FSW. The non-symmetric flow pattern about the weld center-line is correctly predicted. The flow patterns on the advancing and retreating sides are different. On the advancing side, a flow pattern with a *sawing* shape is obtained, which correlates well with the experimental data.

The center-line of the particles is coincident with the weld center-line. The alignment of the particle center-line is more obvious when various sets of particles are located at the initial position (Figure 9). From the colored particle simulation, it can be noted that: (a) the joint is created straightly at the center line, (b) no material mixing is observed

using a circular pin, and, (c) the material moves from the retreating side to the advancing side, leaving a discontinuous line at the advancing side. The particle discontinuity is located at a line parallel to the weld line.

$$\mu_{eff} = \frac{1}{\alpha} \sinh^{-1} \left(\left(\frac{Z}{A} \right)^{\frac{1}{n}} \right); Z = \sqrt{\frac{2}{3}} \|\dot{\mathbf{e}}\| \exp \left(\frac{Q}{RT} \right)$$

α	Material constant	5.2E-08 (m ² /N)
A	Material constant	2.24E+12
n	Material constant	4.54
R	Universal gas constant	8.314 (J/K mol)
Q	Activation energy	177876 (J/mol)

Table 1: Sheppard-Wright constitutive model (AA2195-T8).

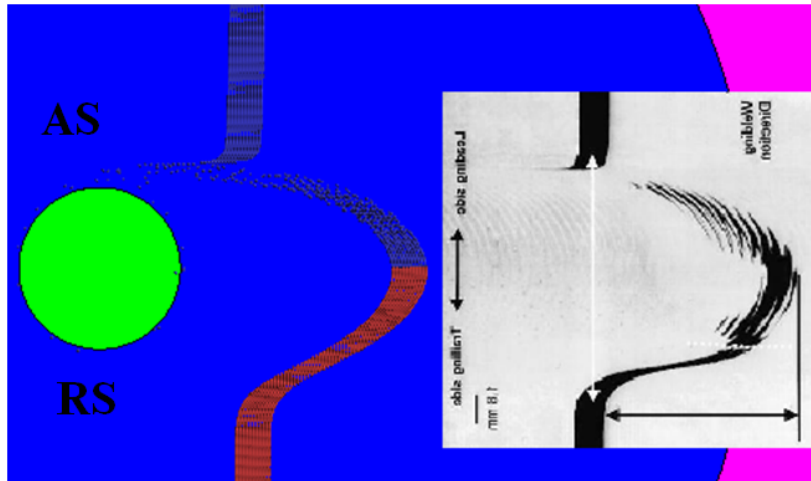


Figure 8: Material flow visualization, current model (left) experiment (right)

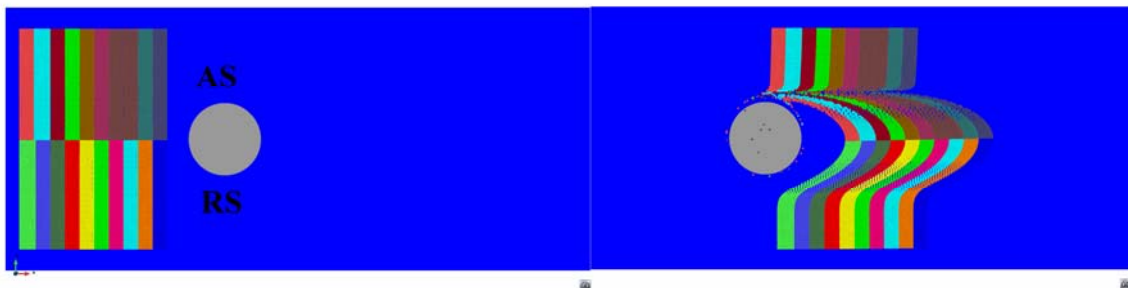


Figure 9: material mixing visualization

4.3. FSW 3D simulation with a threaded pin

Although the 2D simulation agrees well with the experimental results, it does not capture the fully detailed characteristics of the FSW process. To achieve this, a detailed 3D simulation, including the complete tool geometry with shoulder and pin, and pin features such as threads, is considered.

Therefore, the objectives of this simulation are to investigate: (a) the effect of non-axisymmetric pins, particularly, threaded ones, on the material flow behavior, and (b) the effect of the shoulder on the material flow pattern.

To this end, a set of structured material particles in the shape of a rectangular parallel pipe (Figure 1) is traced within the flow. The particles are shown in various colors in order to visualize whether material mixing takes place or not. It also facilitates the visualization of the material particles in different layers in the thickness direction.

The FSW model includes a plate with length, width and thickness of 120 mm, 80 mm and 10 mm, respectively, and a threaded pin shown in Figure 10a. The maximum pin diameter and its length are 10 mm and 9 mm, respectively. The pin has rectangular threads with 1.5 mm pitch. Full stick contact conditions between the pin and the work-piece and between the shoulder and the work-piece are considered. The applied inflow velocity is 5.0833 mm/s. The rotational velocity is 500 rpm. It is prescribed as a constant tangential velocity over the pin volume. The initial and environmental temperatures are 25°C.

The work-piece material is AA2195-T8 with the constitutive model and material properties summarized in Table 1. The pin is made of steel with thermo rigid material properties [13, 14].

The geometry is discretized with a mesh consisting of approximately 80000 linear tetrahedral elements and 82000 nodal points plus 80000 material particles (Figure 11). The mesh density is enhanced around the pin to capture accurately the temperature gradient and strain rate concentration occurring in that zone. Figure 10b shows a magnified view of the mesh discretization on the pin. The problem is solved using the u/p mixed formulation stabilized by the OSS stabilization method [13, 14]. RK4 time integration method is applied for particle tracing.

Figure 12 shows the position of the particles in a millimetric grid background at three (top, middle and bottom) levels of the pin. They are compared to the experimental results taken from Reynolds [20]. The results show that the numerical particle tracing reveals characteristic patterns of the material flow in FSW very accurately. Qualitatively, the flow pattern correlates remarkably well with the experimental data. The non-symmetric flow pattern is correctly predicted. The 3D nature of the flow is demonstrated and simulated with enhanced precision.

Some snapshots of the evolution of the particles movement around the pin at different times are illustrated in Figure 13. Material points initially located in straight lines pass along the tool. Since the shoulder rotates with higher linear velocity than the pin (the radius of the tool shoulder is larger than the radius of the pin), additional friction heat is generated at the top surface. The higher temperature near the top surface makes the material soften to a higher extent. The softened material, together with the advancing inflow, is transported along with the rotating pin from the retreating side to the advancing side. A small amount of the material moves even backwards on the advancing side of the tool center where the flow pattern breaks up. This can be explained by the fact that on the advancing side, the rotational and the advancing velocity fields of the flow have opposite directions while they have the same direction on the retreating side. Therefore, material particles on the advancing side spend a longer time rotating with the pin than on the retreating side.

It can be observed that the radius of curvature of the material flow patterns increases as the material layer is closer to the top surface. The movement of the particles is centrifugal along the thickness direction as they pass through the conical region surrounding the rotating pin tool. This is justified by the full stick contact condition between pin shoulder and work-piece. Because of this, the velocity field mimics the

conical shape. Figure 14 illustrates two vertical cuts across the thickness with velocity contour lines. The larger is the pin diameter, the greater is the velocity and displacement of the material in the weld region.

Figure 13 shows that the extent of mixing of the particles of different colors is minor. This indicates that very limited material mixing occurs. The flow pattern shows that the material mixing happens only at the top of the weld, where the material transport is directly affected by the rotating tool shoulder. Moreover, the interface between the advancing and retreating sides behind the pin is not necessarily maintained at the centerline. For instance, wherever the influence of the rotating shoulder is significant, several particles cross the center-line and material mixing occurs.

During the FSW process, several particles undergo more than one full revolution around the rotating pin. Because of the threaded shape of the tool, a considerable amount of material is shifted from the retreating side to the advancing side causing stirring in the thickness direction. In addition, the forging action combined with the stirring action of the welding tool at the top surface produces a secondary, down-and-up motion of material under the tool. The material in direct contact with the pin is driven downwards due to a combined action of the pin thread and rotation of the pin. Since the material flow in the FSW is a constant volume process, the flow path is constrained. Thus, the material transported to the bottom zone is obliged to move upwards at a certain distance from the pin surface after filling out the potential cavity at the bottom. This way the constant volume constraint is enforced. Figure 15 shows a schematic illustration of the flow of plasticized material adjacent to the threaded pin during FSW.

The z-displacement (vertical) contour field at time 6 s (Figure 16) shows the particles movement in the thickness direction. Due to the high rotational velocity applied to the pin, the values of z-displacement are small in comparison with the displacements in the other directions. The particles located at the bottom of the pin move upwards, contrariwise to the majority, moving downwards. Figure 17 illustrates the z-displacement evolution of two points located at the bottom and mid-height of the pin. Their initial coordinates are (0.0159, -0.0041, -0.0034) and (0.0135, -0.0101, -0.0093), respectively. Note that the particle located at the bottom of the pin moves upwards, following the pin movement. However, the particle in the mid-height moves downwards and, after several revolutions, remains at its new location.

These results reveal the 3D nature of the material flow, in close agreement with the experimental evidence. They prove that numerical particle tracing is a robust tool useful to gain insight into FSW processes.

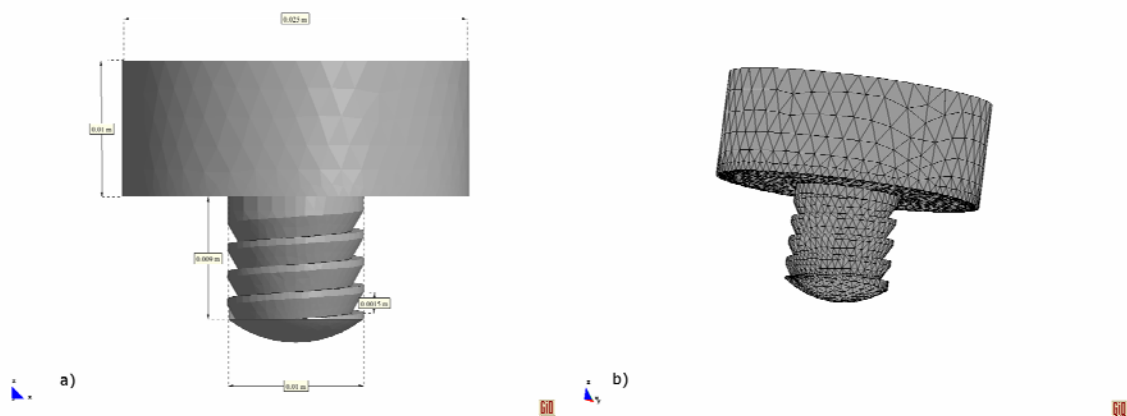


Figure 10: a) Schematic description of the pin geometry; b) Mesh discretization on the pin

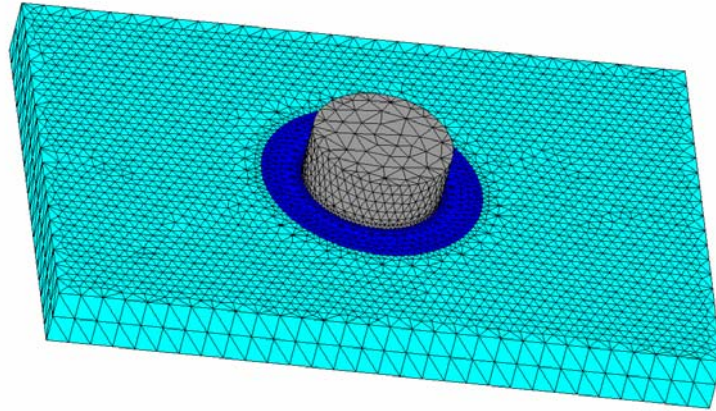


Figure 11: Mesh discretization

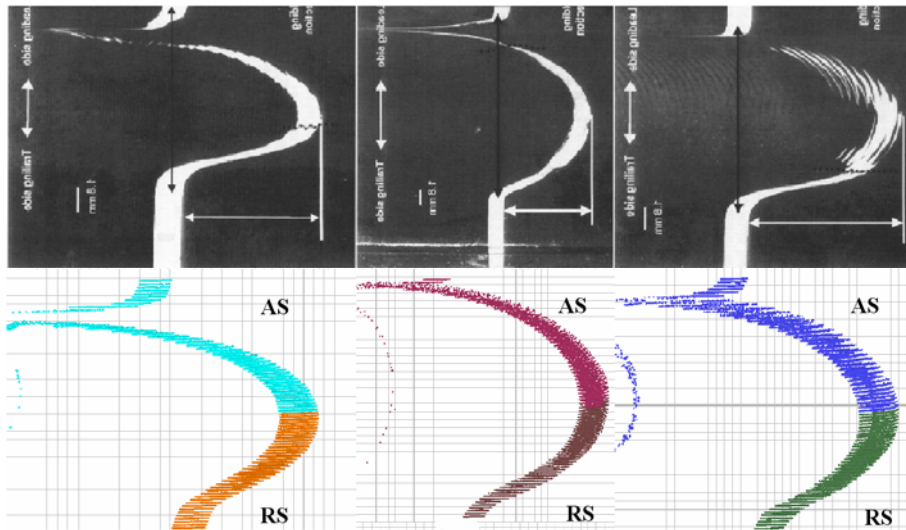
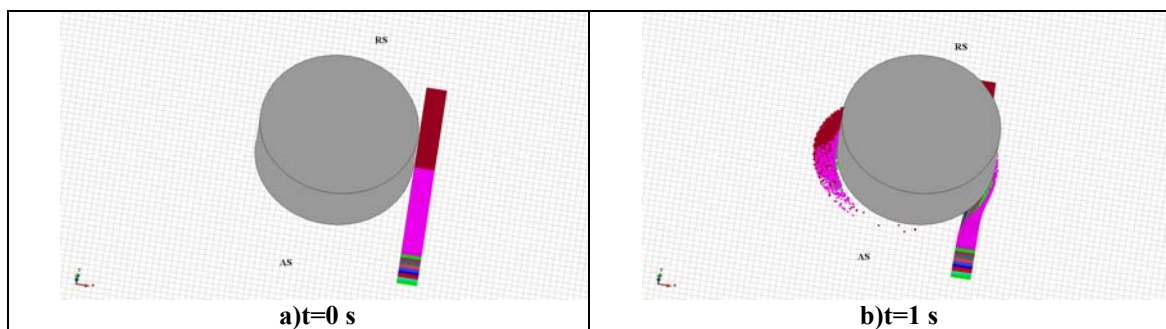


Figure 12: Material pattern at middle, top and bottom level (left to right)



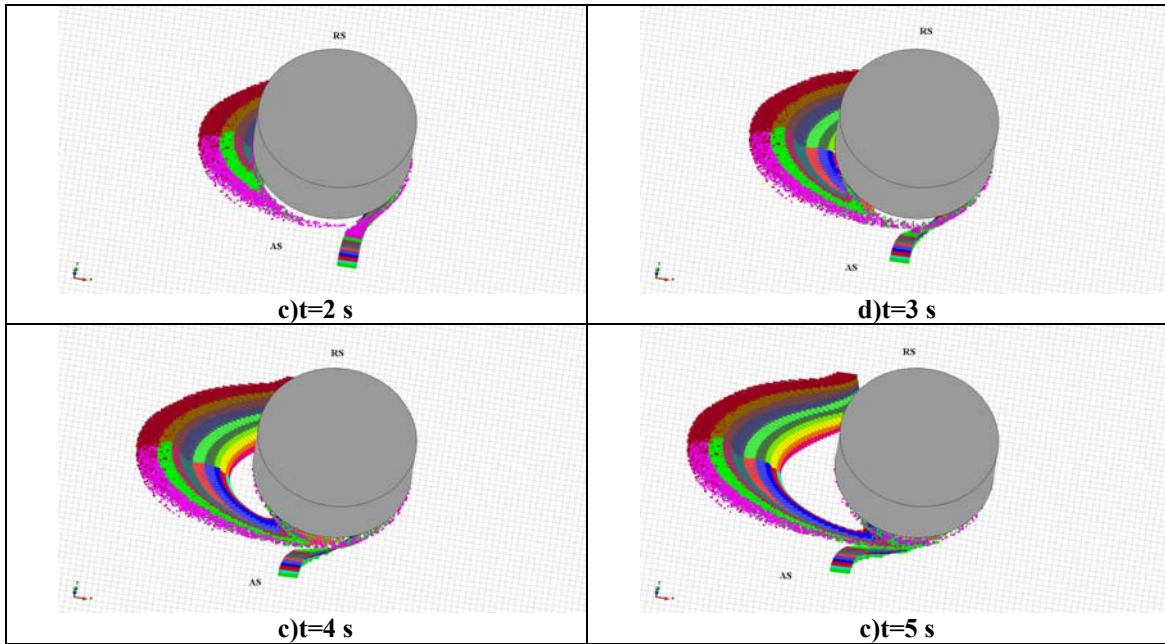


Figure 13: Snapshots of particles movement around the threaded pin

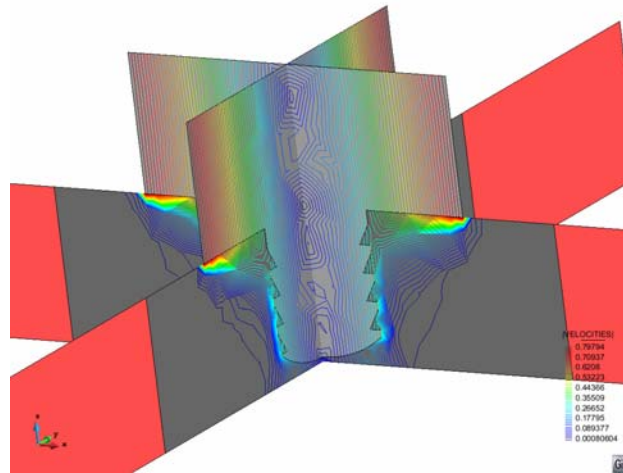


Figure 14: Velocity contour lines on the thickness taken from two vertical cuts

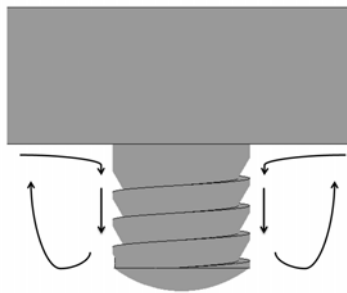


Figure 15: Schematic illustration of the flow of plasticized material adjacent to the threaded pin during FSW using a right-hand threaded pin tool rotating anti-clockwise.

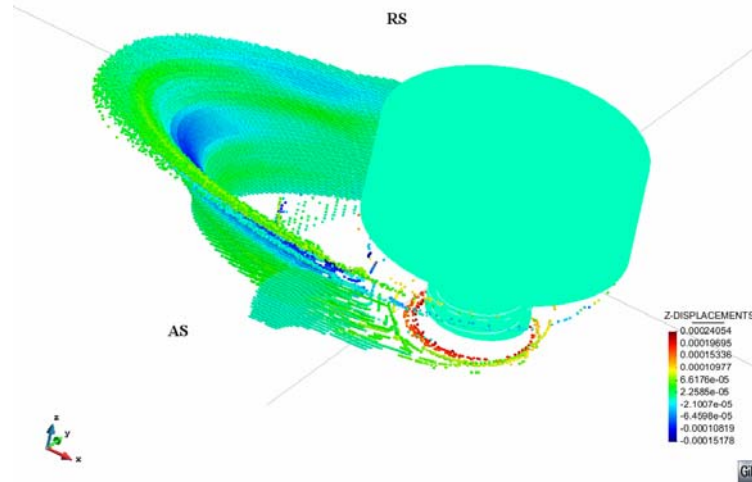


Figure 16: Z-displacement contour field

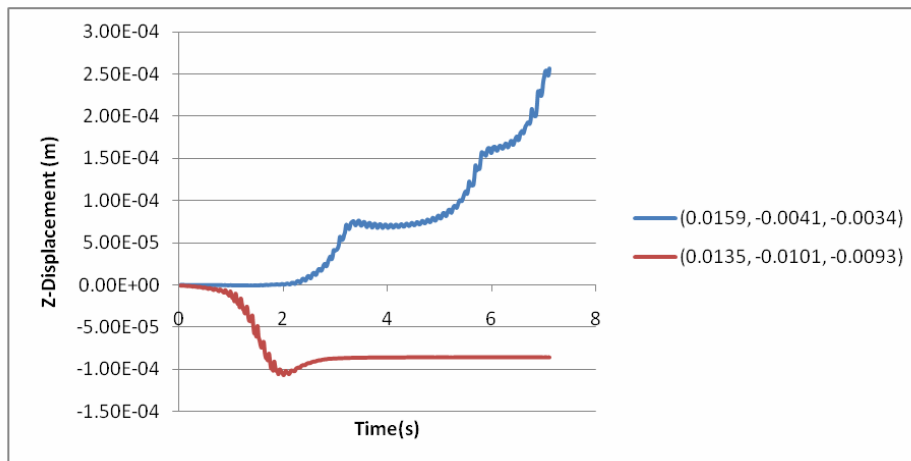


Figure 17: Z-displacement of 2 particles located at bottom and mid-height of the pin

5. Conclusion

In this work, a numerical procedure for the visualization of material flow during the FSW process is presented. A particle tracing technique is applied to track particle trajectories. This is done at the post process level, once the velocity field is obtained. Several integration methods including RK4, BFECC and BES methods are introduced for the problem of interest and compared. Applied to the well-known Zalesak's disk test, it is found that, for large time steps, RK4 is rather accurate while all the other methods fail.

The proposed method is validated comparing the results of a 2D FSW model to experimental data. The 2D simulation shows that the material flow is not symmetric about the joint line. The flow patterns on the advancing and retreating sides are different. The joint is created straightly at the center line and no material mixing is observed. These results are found to be in agreement with experimental data.

The particle tracing method is also applied to a 3D simulation including the complete tool geometry and threaded pin. The 3D simulation shows some distinctive 3D features of the flow. For instance, the material flow around the pin has a centrifugal shape across the thickness. The material stirred on the advancing side performs more than one

revolution around the tool. The up and down movement of the material in the thickness direction is observed.

In both 2D and 3D simulations, agreement with experimental evidence is remarkably good, showing that particle tracing is a useful tool to gain insight of the FSW process.

Acknowledgment

This work was supported by the European Research Council under the Advanced Grant: ERC-2009-AdG “Real Time Computational Mechanics Techniques for Multi-Fluid Problems”. The authors are also thankful for the financial support of the Spanish Ministerio de Educación y Ciencia (PROFIT programme) within the project CIT-020400–2007-82.

References

[1] W.M. Thomas, E.D. Nicholas, J.C. Needham, M.G. Murch, P. Temple-Smith and C.J. Dawes. Friction -stir butt welding. GB Patent No. 9125978.8, International Patent No. PCT/GB92/02203, 1991.

[2] R.S. Mishra and Z.Y. Ma, Friction stir welding and processing, *Materials Science and Engineering R* 50 (2005) 1-78.

[3] B. London, M. Mahoney, B. Bingel, R. Calabrese, D. Waldron, Experimental methods for determining material flow in friction stir welds, The third International symposium on Friction Stir Welding, Kobe, Japan, 27-28 September, 2001.

[4] A.P Reynolds, Flow visualization and simulation in FSW, *Scripta Materialia*, 58 (2008), 338-342.

[5] T. U. Seidel and A.P. Reynolds, Visualization of the material flow in AA2195 Friction Stir Welds using a marker insert technique, *Metallurgical and Materials Transaction A32* (2001) 2879-2884.

[6] K. Colligan, Material Flow Behaviour during Friction Stir Welding of Aluminium, *Welding Journal* 78 (1999) 229-237.

[7] M. Guerra, C. Schmits, J.C. McClure, L.E. Murr and A.C. Nunes, Flow patterns during friction stir welding", *Material Characterization* 49 (2003) 95-101.

[8] T. Dickerson, H.R. Shercliff, H. Schmidt, A weld marker technique for flow visualization in friction stir welding, 4th International Symposium on Friction Stir Welding, Park City, Utah, USA, 14-16 May 2003.

[9] T. Kallgren, L.-Z. Jin, R Sandstrom, Material Flow during Friction Stir Welding of Copper 7th international Friction Stir Welding symposium, Awaji island, Japan, 20-22 May 2008.

[10] R. Johanson, P. Threadgill, Friction Stir Welding of Magnesium alloys, *Magnesium Technology 2003*, TMS, 2003.

[11] J. Ouyang, E. Yarrapareddy, R. Kovacevic, Microstructural evolution in the friction stir welded 6061 aluminum alloy (T6-temper condition) to copper, *Journal of Materials Processing Technology*, 172 (2006) 110-122.

[12] A. Abdollah-Zadeh, T. Saeid, B. Sazgari, Microstructural and mechanical properties of friction stir welded aluminum/copper lap joints, *Journal of alloys and Compounds*, 460 (2008) 535-538.

[13] M. Chiumenti, M. Cervera, C. Agelet de Saracibar and N. Dialami, Numerical Modeling of Friction Stir Welding Processes, *Computer Methods in Applied Mechanics and Engineering* 254 (2013) 353-369. DOI: <http://dx.doi.org/10.1016/j.cma.2012.09.013>

- [14] N. Dialami, M. Chiumenti, M. Cervera and C. Agelet de Saracibar, *Computers and structures* 117, (2013) 48-57. <http://dx.doi.org/10.1016/j.compstruc.2012.12.006>
- [15] T. Dupont and Y.-J. Liu. Back and forth error compensation and correction methods for removing errors induced by uneven gradients of the level set function. *J. Comput. Phys.*, 183 (2002) 83-116.
- [16] S. Osher and R. Fedkiw. *Level Set Methods and Dynamic Implicit Surfaces*. Springer-Verlag, New York, NY, 2002.
- [17] S. Osher and J. Sethian. Fronts propagating with curvature-dependent speed: Algorithms based on Hamilton-Jacobi formulations. *J. Comput. Phys.*, 79 (1988) 12-49.
- [18] J. Donea and A. Huerta, *Finite element method for flow problems*. J. wiley edition, 2003.
- [19] S. T. Zalesak, Fully multidimensional flux-corrected transport, *J. Comput. Phys.*, 31 (1979) 335-362.
- [20] A.P. Reynolds, Visualisation of material flow in autogenous friction stir welds, *Science and technology of welding & joining*. 5(2) (2000) 120-124.
- [21] C. Agelet de Saracibar, M. Cervera, M. Chiumenti, On the formulation of coupled thermoplastic problems with phase-change, *Int. J. Plasticity* 15 (1999) 1-34.
- [22] M. Cervera, C. Agelet de Saracibar, M. Chiumenti, Thermo-mechanical analysis of industrial solidification processes, *Int. J. Numer. Methods Engrg.* 46 (1999) 1575-1591
- [23] F. Brezzi, M. Fortin, *Mixed and Hybrid Finite Element Methods*, Springer, New York, 1991.
- [24] C. Agelet de Saracibar, M. Chiumenti, Q. Valverde, M. Cervera, On the orthogonal subgrid scale pressure stabilization of finite deformation J2 plasticity, *Comput. Methods Appl. Mech. Engrg.* 195 (2006) 1224-1251.
- [25] M. Cervera, M. Chiumenti, Q. Valverde, C. Agelet de Saracibar, Mixed linear/linear simplicial elements for incompressible elasticity and plasticity, *Comput. Methods Appl. Mech. Engrg.* 192 (2003) 5249-5263.
- [26] M. Chiumenti, Q. Valverde, C. Agelet de Saracibar, M. Cervera, A stabilized formulation for incompressible plasticity using linear triangles and tetrahedra, *Int. J. Plasticity* 20 (2004) 1487-1504.